applied sciences

MDPI

Article

Modeling and Characteristic Analysis of Combined Beam Tri-Stable Piezoelectric Energy Harvesting System Considering Gravity

Xuhui Zhang [1,2,*], Hengtao Xu [1], Jianan Pan [1], Xiaoyu Chen [1], Fulin Zhu [1], Yan Guo [1], Hao Tian [1] and Yujun Cheng [1]

[1] College of Mechanical Engineering, Xi'an University of Science and Technology, Xi'an 710054, China
[2] Shaanxi Key Laboratory of Mine Electromechanical Equipment Intelligent Monitoring, Xi'an University of Science and Technology, Xi'an 710054, China
* Correspondence: zhangxh@xust.edu.cn

Abstract: The emergence of the vibration energy harvesting system makes it possible for wireless monitoring nodes in coal mines to realize self-power supply. In order to reveal the influence of gravity effect on the response characteristics of the combined beam tri-stable piezoelectric energy harvesting system (CTEHS), the system's nonlinear magnetism is calculated according to the principle of point magnetic charge dipole, and the system's nonlinear resilience is obtained through experimental measurements and nonlinear fitting methods. Based on the Lagrange equation, the system's electromechanical coupling motion model considering gravity is established. The system's motion equation is solved numerically based on the Runge–Kutta algorithm, and the effects of the end magnet mass and the initial vibration point on the bifurcation behavior, potential energy, and system output performance are investigated by emulation and experiment. The research shows that the magnet's gravity effect causes a change in the stable equilibrium position and the system's motion state and also causes the system to generate additional gravitational potential energy, which leads to a potential asymmetric well of the system. Under the consideration of magnet gravity, the appropriate end magnet mass and initial vibration point can not only reduce the system's requirements for external excitation strength but also effectively improve the system's response and output. This research provides a new theoretical basis for the optimal design of the tri-stable piezoelectric energy harvesting system.

Keywords: tri-stable; magnetic coupling; gravity effect; asymmetric potential well; response characteristics

check for updates

Citation: Zhang, X.; Xu, H.; Pan, J.; Chen, X.; Zhu, F.; Guo, Y.; Tian, H.; Cheng, Y. Modeling and Characteristic Analysis of Combined Beam Tri-Stable Piezoelectric Energy Harvesting System Considering Gravity. *Appl. Sci.* **2023**, *13*, 94. https://doi.org/10.3390/app13010094

Academic Editor: Yoshiyasu Takefuji

Received: 21 November 2022
Revised: 19 December 2022
Accepted: 20 December 2022
Published: 21 December 2022

1. Introduction

In the latest years, with the fast development of wireless monitoring and microelectronics technology, wireless monitoring systems have shown strong application potential in monitoring fields such as ecological environment [1], equipment status [2], and traffic safety [3]. Most of the current wireless monitoring nodes use battery power; however, chemical batteries are not only difficult to recycle but also need to be replaced regularly and have high maintenance costs. Vibration energy harvesting technology can achieve the transformation of vibration energy into electric energy, which provides new ideas and methods to handle the endurance problem of wireless monitoring nodes [4,5].

At present, the vibration energy capture method by using the piezoelectric principle has become the research hotspot due to its advantages of easy miniaturization, simple structure and high energy density [6–8]. The researchers initially mainly studied the linear piezoelectric energy capture system and characterized the system's motion characteristics by establishing a linear mathematical model. However, as far as the linear piezoelectric energy harvesting system [9] is concerned, only when the vibration frequency is near the intrinsic frequency of the system structure can the system produce an efficient output. The excitation frequency of the real external environment is often random, has a certain range, and cannot always be near the intrinsic frequency of the system. As a result, the electricity generation efficiency of the linear piezoelectric energy capture system is low, and it is difficult to be widely used. In order to broaden the effective operating frequency band of the piezoelectric energy capture system and improve the energy capture performance of the system, researchers introduced nonlinear factors on the basis of the linear energy capture system and began to explore and study the nonlinear piezoelectric energy harvesting system [10,11]. The nonlinear energy harvesting systems currently studied are mainly realized by introducing nonlinear stiffness. There are three main methods for introducing nonlinear stiffness, which are external force coupling [12,13], piecewise linear [14,15], and nonlinear strain [16,17]. Compared with the other two methods, external force coupling has the advantages of strong reliability and easy realization and is the current key research direction [18].

As the most common way of external force coupling, the introduction of nonlinear magnetism can make the system achieve a large response in monostable [19,20], bistable [21,22], and multistable [23,24]. Researchers have conducted a great deal of research on the piezoelectric energy capture system using this way [25–27]. Fan [28] proposed a monostable piezoelectric energy capturer by introducing a set of symmetrical attracting magnets outside the cantilever beam. The research results indicated that the energy harvesting bandwidth and output voltage of the system are greatly improved compared with the linear system. Xie [29] proposed an asymmetric double-beam monostable piezoelectric energy harvester and found that the asymmetric structure has higher output performance and harvesting efficiency than the symmetric structure. Ferrari [30] arranged two mutually repelling magnets at the tip and outside to form a bistable piezoelectric energy harvester. Through experimental tests, it was found that the introduction of magnetism significantly enhanced the harvesting ability of the bistable energy harvester. Erturk [31] established a nonlinear bistable model by using the attraction of two fixed magnets to the ferromagnetic beam and proved that the bistable system has higher output voltage and power than the linear system through theoretical and experimental studies. Lan [32] designed an improved bistable energy capturer by placing a miniature magnet in the middle of two external magnets, and the analysis results showed that the improved bistable system can achieve high energy output at lower excitation intensity. Zhou [33] proposed a magnetic coupling nonlinear tristable energy harvester. Compared with the bistable system, the tristable system is easier to escape from the potential well and achieve a large response and output. Jung [34] designed a tristable piezoelectric energy capturer with two rotatable magnets and found that with the change of the magnet rotation angle, the motion characteristics of the system also change. Sun [35] improved the structure of the traditional tristable energy capturer and replaced the traditional two external magnets with a ring magnet. Simulation and experiment prove that this ring magnet structure constitutes a tristable system and is completely feasible. Zhou [36] arranged three magnets outside to form a quadstable piezoelectric energy capturer. The experimental study indicated that the quadstable system exhibited richer output response characteristics than the bistable system.

Most of the above research and analysis on the magnetic coupling nonlinear energy harvesting system are carried out under ideal conditions without considering the gravity effect of the system. However, gravity is real and inevitable in the energy harvesting system. Therefore, it is necessary to further explore the influence of gravity effect on the piezoelectric energy harvesting system. For the combined beam tri-stable piezoelectric energy harvesting system (CTEHS) proposed by this research group, some related studies are carried out in this paper considering the gravity of the end magnets. The remainder of this paper is organized as shown below: In the next section, the overall structure of CTEHS is described first, then the establishment process of the system's magnetism model and resilience model is introduced, and then the system dynamics equation considering gravity is derived by using the Lagrange theorem. In Section 3, the effects of the magnet's gravity on the system's bifurcation behavior and potential well characteristics are first studied, then the effects of different end magnet masses and initial vibration points on the system's output characteristics are researched by numerical emulation. In Section 4, the results of the theoretical study are validated by experimental tests. In the last section, the research results and findings of this paper are refined and summarized.

2. Structure and Mathematical Model of CTEHS

2.1. Structure of CTEHS

The overall structure of CTEHS is shown in Figure 1, which mainly includes a pedestal, combined beam, magnet, and PVDF (polyvinylidene difluoride). The combined beam consists of a linear part and an arch part. The linear end of the combined beam is fastened to the right side of the base, the arched end is connected with magnet 1, and the left side of the base is symmetrically placed with two magnets: 2 and 3. A layer of PVDF piezo sheet adheres to the top side of the beam. PVDF has two electrodes distributed on opposite surfaces. When PVDF is subjected to external force, positive and negative charges will appear on the surface of its two electrodes, thus forming positive and negative electrodes of PVDF. In this paper, the upper surface electrode of PVDF is the positive electrode, and the lower surface electrode is the negative electrode. Both ends of the load resistor R are connected to the positive and negative electrodes of PVDF through wires. When the pedestal is subjected to external vibration in the z-orientation, the end magnets of the combined beam will produce a corresponding displacement, which will deform the combined beam. According to the piezoelectric effect, the top and bottom surfaces of the PVDF piezoelectric film will generate a definite volume of electric energy. In Figure 1, L is the lateral length of the combined beam along the x-orientation, d_h is the horizontal spacing between the end magnet 1 and the external magnets 2 and 3, and d_v is the vertical spacing between the external magnets 2 and 3.

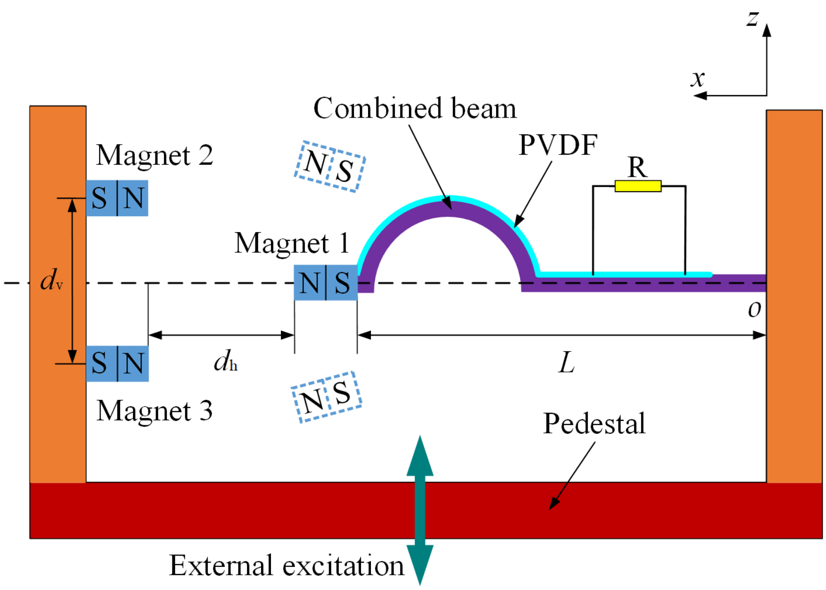

Figure 1. Overall schematic diagram of CTEHS.

2.2. Mathematical Model of CTEHS

2.2.1. Magnetism Model

In order to study the output performance of CTEHS, the nonlinear magnetism model of the system must be established first. In this research, the magnetism between magnets is calculated and modeled according to the point magnetic charge dipole theory. Figure 2 shows the geometric positions and relations of magnets 1, 2, and 3.

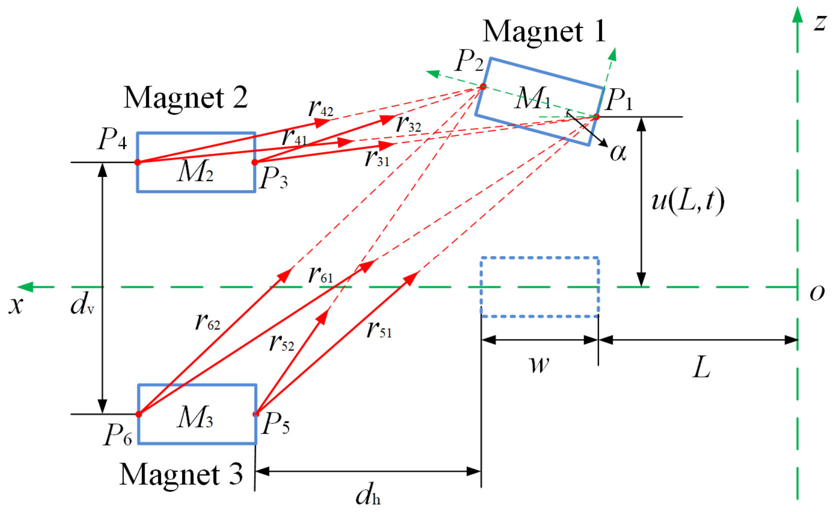

Figure 2. Geometric positions and relations of the magnet.

In Figure 2, M_1, M_2, and M_3 are the magnetization of the three magnets, $P_i(i = 1,2,3,4,5,6)$ is the dipole point of the magnet, $r_{ij}(i = 3,4,5,6,\ j = 1,2)$ is the orientation vector of the point dipole, w is the transverse length of the three magnets, $u(L,t)$ is the response displacement of the end magnet 1 in the z-direction, and α is the rotation angle of the end magnet 1. Based on the point magnetic charge dipole method, the magnetism between magnet 1 and magnet 2 can be obtained as

$$F_{12} = \frac{Q_{12}}{4\pi}\left(-\frac{\delta_1}{((d_h+w)^2+\delta_1^2)^{\frac{3}{2}}} + \frac{\delta_1}{((d_h+2w)^2+\delta_1^2)^{\frac{3}{2}}} + \frac{\delta_2}{(d_h^2+\delta_2^2)^{\frac{3}{2}}} - \frac{\delta_2}{((d_h+w)^2+\delta_2^2)^{\frac{3}{2}}}\right) \tag{1}$$

where $Q_{12} = \mu_0 M_1 S_1 M_2 S_2$, $\delta_1 = u(L,t) - d_v/2$, $\delta_2 = u(L,t) + \alpha w - d_v/2$. S_1, S_2 are the surface areas of magnets 1,2 in the z-direction, and μ_0 is the magnetic permeability under vacuum conditions.

Similarly, the magnitude of the magnetism between magnet 1 and magnet 3 is

$$F_{13} = \frac{Q_{13}}{4\pi}\left(-\frac{\delta_3}{((d_h+w)^2+\delta_3^2)^{\frac{3}{2}}} + \frac{\delta_3}{((d_h+2w)^2+\delta_3^2)^{\frac{3}{2}}} + \frac{\delta_4}{(d_h^2+\delta_4^2)^{\frac{3}{2}}} - \frac{\delta_4}{((d_h+w)^2+\delta_4^2)^{\frac{3}{2}}}\right) \tag{2}$$

where $Q_{13} = \mu_0 M_1 S_1 M_3 S_3$, $\delta_3 = u(L,t) + d_v/2$, $\delta_4 = u(L,t) + \alpha w + d_v/2$.

Therefore, the total magnetism between the three magnets is

$$F_m = F_{12} + F_{13} \tag{3}$$

2.2.2. Resilience Model

Since the resilience of the combined beam is complex, the resilience of the system is modeled by experimental measurement and polynomial fitting in this paper. The specific implementation process is as follows: first, one end of the combined beam is fastened, and the other end is pushed using an ergometer (YLK-10) to gauge the resilience data of the combined beam, then multiple measurements are taken and averaged, and finally, the resilience model of the system is obtained by polynomial fitting. The relationship between resilience F_r and displacement $u(L,t)$ is expressed as follows

$$F_r = k_1 u^3(L,t) + k_2 u(L,t) \tag{4}$$

The coefficients k_1 and k_2 in Equation (4) are obtained by polynomial fitting the measured resilience and displacement data with MATLAB. The coefficient $k_1 = -54715.8\ \mathrm{N/m^3}$, $k_2 = -19.65\ \mathrm{N/m}$ in Equation (4). Figure 3 shows the experiment data and fitting curve of the displacement–resilience of the combined beam. It can be found from Figure 3 that the resilience of the combined beam is nonlinear, and the fitted curve is in good agreement with the experimentally measured data.

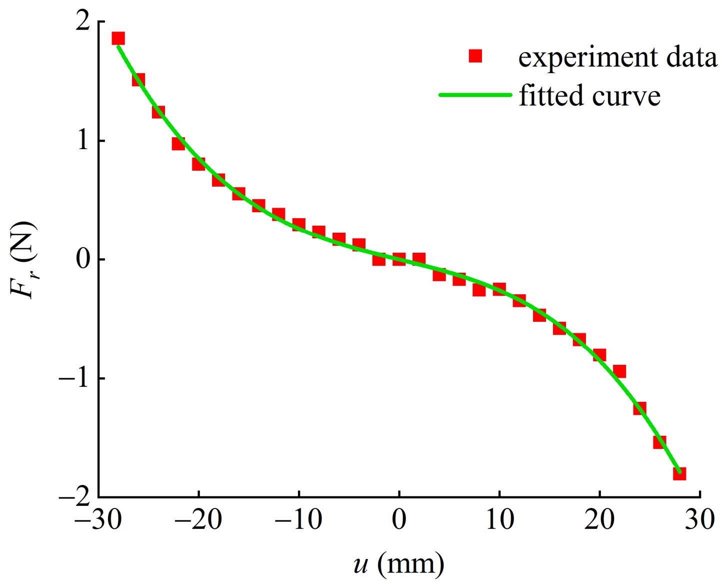

Figure 3. Resilience fitting results.

2.2.3. Motion Equation of CTEHS

In this research, the motion equation of CTEHS considering the gravity effect is established based on the Lagrange equation. The Lagrange function of the system is as follows

$$L_a = T_l + T_m + W_p - U_r - U_m - U_g \tag{5}$$

where T_l is the kinetic energy of the combined beam and PVDF, T_m is the kinetic energy of magnet 1, W_p is the electric energy produced by the PVDF, U_r is the resilient potential energy of the combined beam and PVDF, U_m is the magnetism potential energy between three magnets, and U_g is the gravitational potential energy of the magnet 1. The following are the specific manifestations of these energies:

$$T_l = \frac{1}{2}(\rho_p A_p + \rho_b A_b)\int_0^L \left[\frac{\partial u(x,t)}{\partial x} + \dot{y}(t)\right]^2 dx \tag{6}$$

$$T_m = \frac{1}{2}M_e\left\{\left[\frac{\partial u(x,t)}{\partial t}\right]_{x=L} + \dot{y}(t)\right\}^2 + \frac{1}{2}I_e\left[\frac{\partial^2 u(x,t)}{\partial t \partial x}\right]^2_{x=L} \tag{7}$$

$$W_p = \frac{1}{4}e_{31}k_p(h_b + h_p)V(t)\left[\frac{\partial u(x,t)}{\partial x}\right]_{x=L} + \frac{1}{2}C_p V^2(t) \tag{8}$$

$$U_r = \int F_r \mathrm{d}u(L,t) \tag{9}$$

$$U_m = \int F_m \mathrm{d}u(L,t) \tag{10}$$

$$U_g = F_g u(L,t) = M_e g u(L,t) \tag{11}$$

where ρ_b, ρ_p are the material densities of the combined beam and PVDF, A_b, A_p are the cross-section areas of the combined beam and PVDF, and h_b, h_p are the thicknesses of the combined beam and PVDF, respectively. $\dot{y}(t)$ is the vibration velocity of the base, M_e, I_e are the mass and moment of inertia of the end magnet 1, respectively, $V(t)$ is the response voltage of PVDF, e_{31}, C_p are the piezoelectric constants and equivalent capacitance of PVDF, respectively.

The end vibration displacement $u(x,t)$ of the combined beam can be expressed according to the Galerkin method as

$$u(x,t) = \sum_{i=1}^{N} \psi_i(x)\gamma_i(t) \tag{12}$$

where $\psi_i(x), \gamma_i(t)$ express the i-th mode shape function and modal coordinates of the combined beam, respectively. The research in this paper is mainly aimed at low-frequency vibration. Therefore, we only take into account the 1st-order modalities of the beam, and the specific expression of the mode shape function $\psi(x)$ is

$$\psi(x) = 1 - \cos\left(\frac{\pi x}{2L}\right) \tag{13}$$

Combining all the above equations, the electromechanical coupling motion equation of the system considering gravity can be obtained as follows:

$$\begin{cases} M\ddot{\gamma}(t) + C\dot{\gamma}(t) + F_r - \Theta V(t) + F_m + F_g = -\beta\ddot{y}(t) \\ \Theta\dot{\gamma}(t) + V(t)/R + C_p\dot{V}(t) = 0 \end{cases} \tag{14}$$

where

$$M = \left(\rho_p A_p + \rho_b A_b\right)\int_0^L \psi^2(x)\mathrm{d}x + M_\mathrm{e}\psi^2(L) + I_\mathrm{e}\left(\psi'(L)\right)^2 \tag{15}$$

$$\Theta = \frac{1}{2}e_{31}k_p\left(h_p + h_b\right)\psi'(L) \tag{16}$$

$$\beta = \left(\rho_p A_p + \rho_b A_b\right)\int_0^L \psi(x)\mathrm{d}x + M_\mathrm{e}\psi(L) \tag{17}$$

$$\ddot{y}(t) = A\cos(2\pi f t) \tag{18}$$

In Equation (18), A is the acceleration amplitude of the external vibration, and f is the frequency of the external vibration.

3. Simulation Analysis of CTEHS

3.1. Analysis of Bifurcation Characteristics of System Static Solution

3.1.1. Influence of End Magnet Mass M_e on the (d_h, u) Bifurcation Diagram

Table 1 lists the specific parameters of the system components used in the numerical simulation.

Table 1. Simulation parameters of the system.

Component	Parameter	Value	Unit
Combined Beam part	Length	40	mm
	Width	8	mm
	Thickness	0.2	mm
	Density	8300	kg/m^3
	Young's Modulus	128	GPa
PVDF part	Length	40	mm
	Width	8	mm
	Thickness	0.11	mm
	Density	1780	kg/m^3
	Young's Modulus	3	GPa
	Piezoelectric Stress Constant	−11.5	C/m^2
Magnet part	Length	10	mm
	Width	10	mm
	Thickness	5	mm
	Mass	3.75	g
	Magnetization Intensity	4.5×10^5	A/m

Let $\ddot{\gamma}(t) = \dot{\gamma}(t) = \dot{V}(t) = V(t) = \ddot{y}(t) = 0$ in the system's motion equation, then the system's equation in a static state is

$$F_r + F_m + F_g = 0 \tag{19}$$

It can be found from Equation (19) that the static solution of the system depends not only on the nonlinear magnetism and resilience of the system but also on the gravity of the end magnets. The system's static bifurcation diagram, under the consideration of the end magnet's gravity, can be obtained by solving Equation (19).

First, the influence of end magnet mass M_e on the system's bifurcation behavior is studied in (d_h, u) plane. Taking d_v = 20 mm, M_e = 0,3,6,9,12,15 g, the bifurcation diagram of the system in the (d_h, u) plane is shown in Figure 4, where the real lines represent the stable solution and the dotted lines represent the unstable solution. Figure 4a is the bifurcation diagram when M_e= 0 g, that is, the gravity of the end magnet is not considered, and two saddle points S symmetrical about u = 0 appear in the system. When $d_h > d_{hS}$, there is just one zero-point solution to the static equation. When $d_h < d_{hS}$, there exist three stable solutions and two unstable solutions of the static equation, the system shows as a tristable system at this time. When M_e = 3 g, as shown in Figure 4b, under the influence of the gravity of the magnet, the bifurcation diagram presents asymmetry up and down. The upper saddle point shifts to the left to point S_1, and the lower saddle point shifts to the right to point S_2, and the zero stable position of the system is shifted downward, and the offset is Δu. When $d_h > d_{hS1}$, there is just one solution to the static equation, and the gravity effect of the magnet makes this stable solution negative, at which time the system is monostable. When $d_{hS1} < d_h < d_{hS2}$, there exist two stable solutions and one unstable solution of the static equation, and the system shows as a bistable state. When $d_h < d_{hS1}$, there exist five solutions to the static equation, and the system exhibits a tristable characteristic in this range.

As shown in Figure 4c,d, when M_e is increased to 6 g and 9 g, the saddle point S_1 continues to move to the left gradually, S_2 continues to move to the right gradually, the middle stable solution continues to shift downward, and the offset Δu becomes larger and larger. In addition, the movement of the saddle points S_1 and S_2 makes the range of the bistable system gradually increase. When M_e = 12 g, as shown in Figure 4e, the middle stable solution continues to move down and coincides with the lower saddle point S_2, forming a fork point P. At this time, the range of the system in a bistable state reaches the maximum. When M_e is increased to 15 g, as shown in Figure 4f, the middle stable solution is separated from the fork point P. The fork point P turns into the saddle point S_2 and moves to the left, and the offset phenomenon of the middle stable solution becomes more obvious.

3.1.2. Influence of End Magnet Mass M_e on the (d_v, u) Bifurcation Diagram

Next, the influence of M_e on the system's bifurcation behavior is studied in (d_v,u) plane. Taking d_h = 10 mm, M_e = 0,5,10,15 g, the bifurcation diagram of the system in the (d_v,u) plane is shown in Figure 5. When M_e = 0 g, as shown in Figure 5a, two symmetrical saddle points, S, and a fork point, P, appear in the system's bifurcation diagram. At this time, the system has a total of three stable and two unstable solutions. When $d_v < d_{vP}$, the system exhibits bistable characteristics, when $d_{vP} < d_v < d_{vS}$, the system is a tristable system, and when $d_v > d_{vS}$, the system behaves in a monostable state. Increase M_e to 5 g, as shown in Figure 5b, the system's bifurcation diagram is no longer symmetrical up and down, the upper saddle point S shifts to the lower left to point S_1, the lower saddle point S shifts to the lower right to point S_2, the fork point P divides into two fork points P_1 and P_2, and the zero stable solution of the system shifts downward. When $d_v < d_{vP2}$, the system behaves as bistable, when $d_{vP2} < d_v < d_{vS1}$, the system exhibits tristable characteristics, when $d_{vS1} < d_v < d_{vS2}$, the system behaves as bistable again, when $d_v > d_{vS2}$, The system is a monostable system.

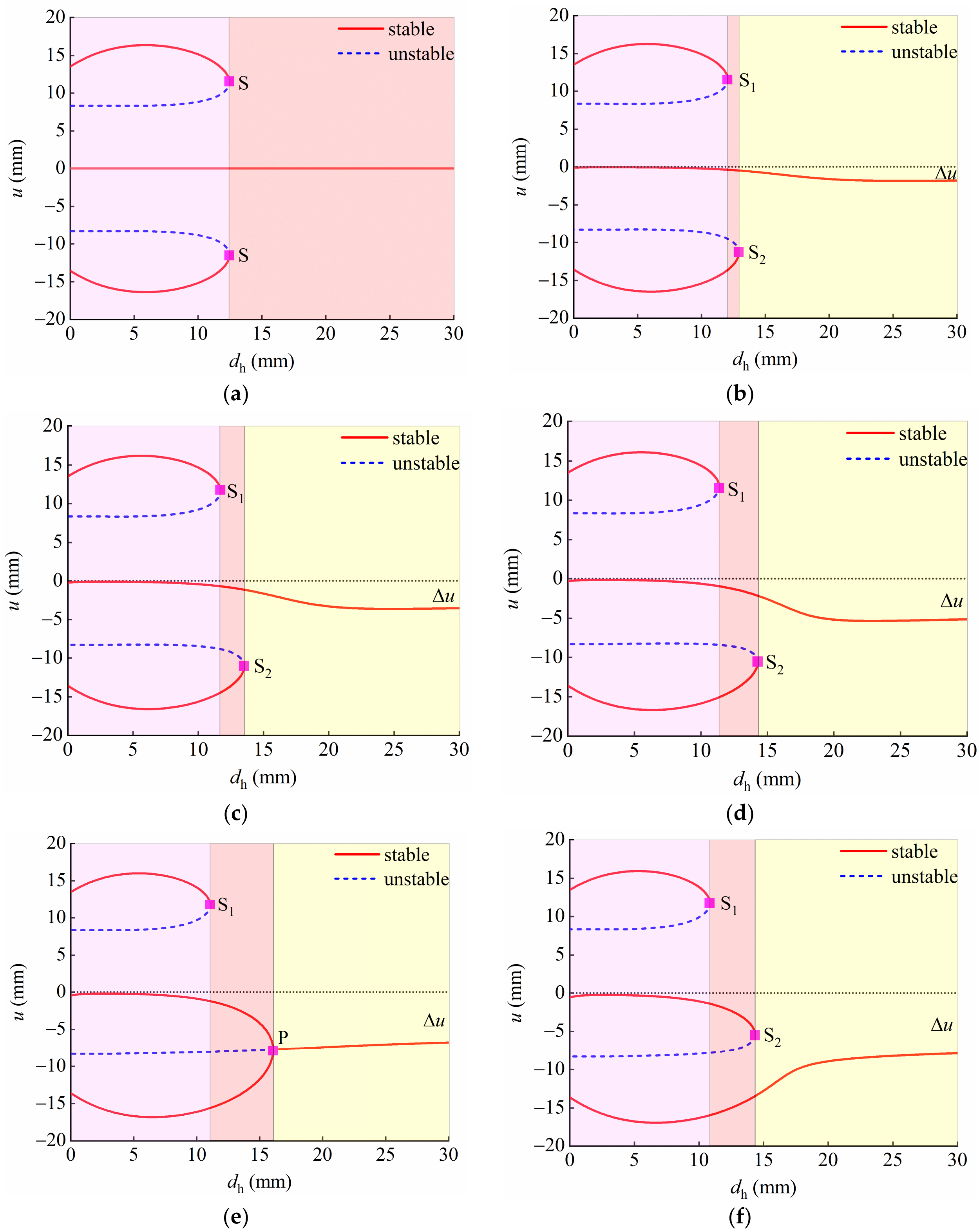

Figure 4. Bifurcation diagram of (d_h, u) with different end magnet masses M_e: (**a**) M_e = 0 g; (**b**) M_e = 3 g; (**c**) M_e = 6 g; (**d**) M_e = 9 g; (**e**) M_e = 12 g; (**f**) M_e = 15 g.

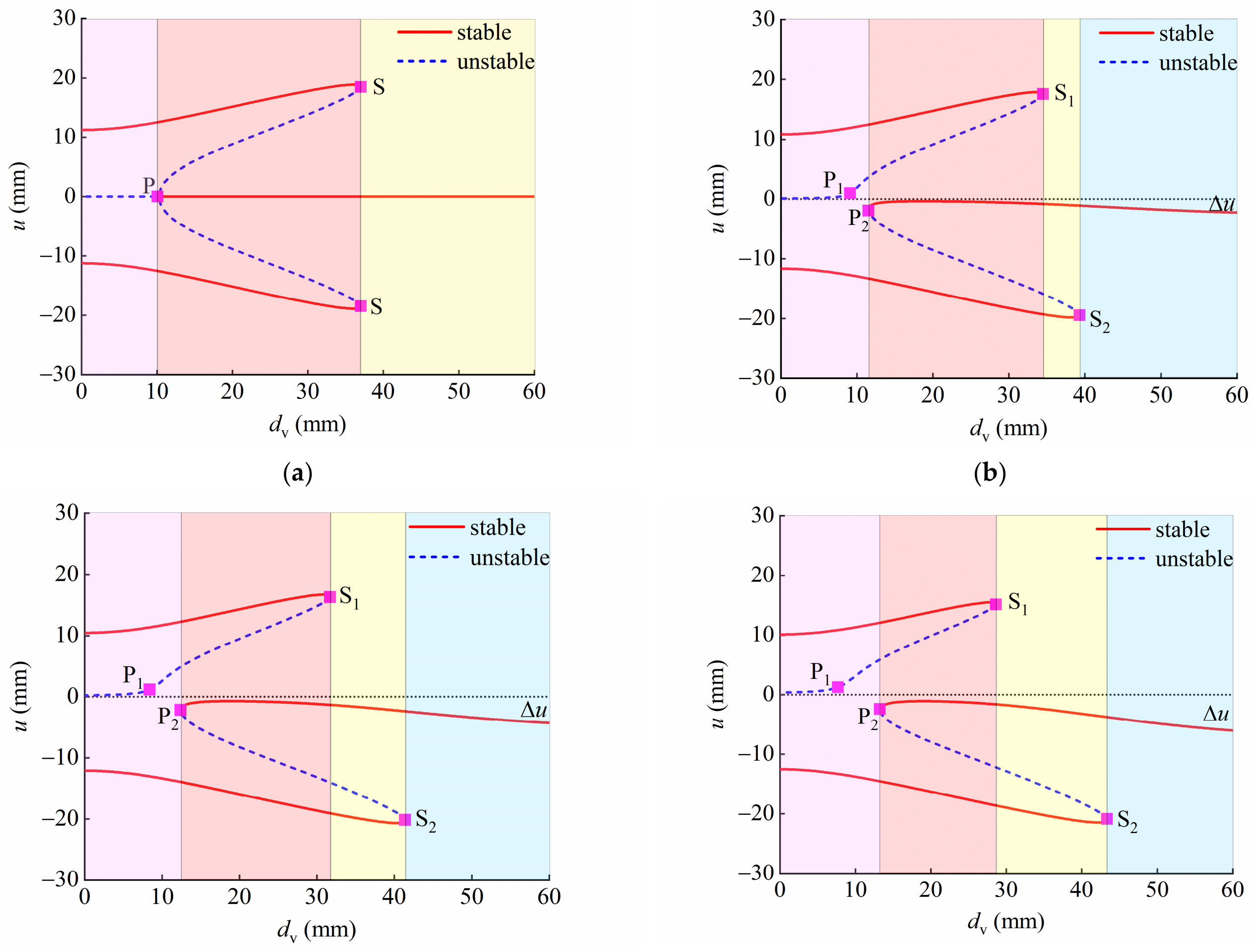

Figure 5. Bifurcation diagram of (d_v, u) with different end magnet masses M_e: (**a**) M_e = 0 g; (**b**) M_e = 5 g; (**c**) M_e = 10 g; (**d**) M_e = 15 g.

Continue to increase M_e to 10 g and 15 g, as shown in Figure 5c,d, the upper saddle point S_1 keeps moving to the lower left and the lower saddle point S_2 keeps moving to the lower right under the action of the magnet gravity. At the same time, the fork point P_1 gradually moves to the left, P_2 gradually moves to the right, and the offset Δu of the middle stable solution becomes larger. The range where the system exhibits a tristable state gradually decreases, and the range where the system exhibits a bistable state gradually increases.

3.2. Analysis of Potential Energy

From Equation (5), the system's potential energy includes the magnetism potential energy and gravitational potential energy generated by magnets, as well as the resilient potential energy of the combined beam, the expression of which is

$$U = U_r + U_m + U_g \tag{20}$$

To study the effect of the end magnet's gravity on the total potential energy of the tristable system, take d_h = 11 mm, d_v = 16 mm, M_e = 0~20 g, according to Equation (20), the 3D potential energy surface of the system with the change of end magnet mass M_e can be drawn as shown in Figure 6. It can be found from Figure 6 that the change law of system potential energy on both sides of u = 0 is opposite. When u < 0, as M_e increases, the system's potential energy decreases gradually. When $u > 0$, the system's potential energy increases gradually with the increase of M_e.

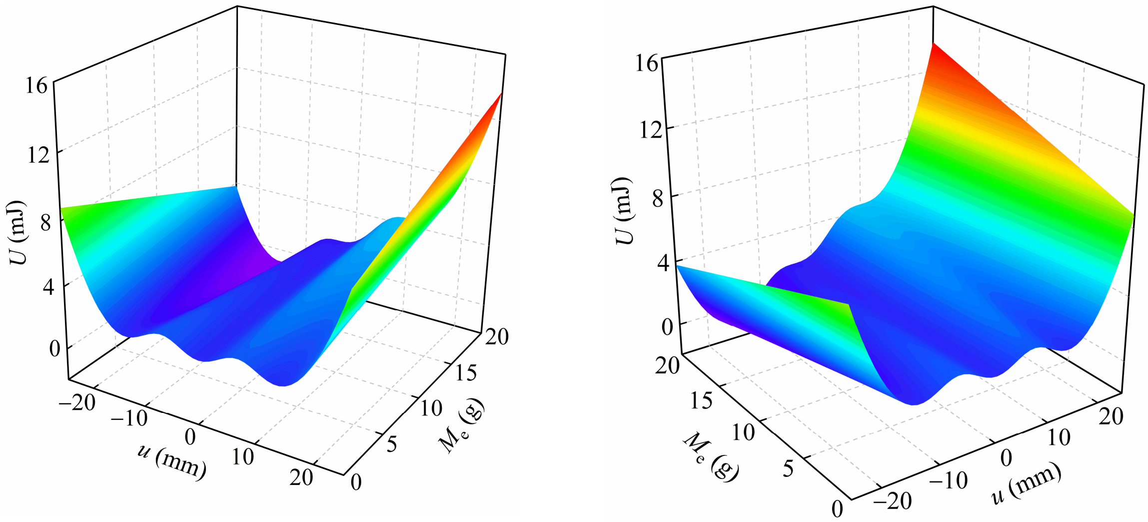

Figure 6. 3D potential energy surface of the system.

To deeply analyze the variation features of the potential energy of the tri-stable system, M_e is taken as 0, 4, 8, 12, and 16 g, respectively. The system's potential energy curves under different M_e are shown in Figure 7. When M_e = 0 g, that is, when the gravity of the magnet is not considered, the system's left and right potential wells have identical shapes, and the potential energy curve is symmetrical about u = 0. When M_e = 4 g, the left potential well of the system moves downward and becomes deeper, the right potential well moves upward and becomes shallower, and the potential energy curve is no longer symmetric. As M_e continues to increase, the system's left potential well continues to move down, the right potential well continues to move up, and the asymmetry of the potential well becomes more and more obvious. In addition, it can be found that under the action of magnet gravity, with the increase of M_e, the lowest points of the system's three potential wells, that is, the system's three stable positions, all gradually move towards the negative half-axis of u. This is accordant with the study results of the system's bifurcation behavior.

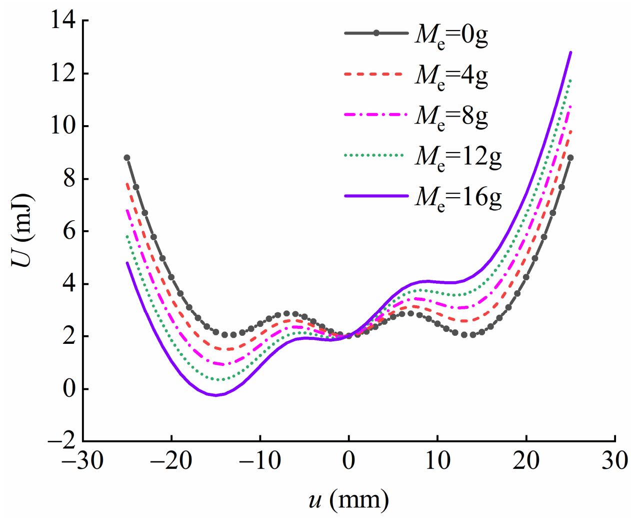

Figure 7. System's potential energy curve under different M_e.

3.3. Analysis of System Response Characteristics

3.3.1. Influence of End Magnet Mass M_e on System Response Characteristics

To investigate the effect of the end magnet's gravity on the system's response characteristics, Equation (14) is solved by using the ODE45 algorithm to derive the system's output response under different initial excitation conditions. Taking d_h = 12 mm, d_v = 15 mm, excitation frequency f = 10 Hz, M_e = 0,4,6,8 g, Figure 8 shows the relation between the system's RMS voltage and the excitation acceleration A under different M_e. As can be found in Figure 8, the system's RMS voltage jumps from low to high as the excitation acceleration A increases. However, when M_e takes different values, the excitation acceleration required for the system to jump is different. When M_e = 0 g, that is, without considering the gravity of the magnet, the acceleration threshold for the system to achieve a large output voltage is 18.6 m/s^2. When M_e is 4, 6, and 8 g, the acceleration thresholds are 13 m/s^2, 10.2 m/s^2, and 7.5 m/s^2, respectively. It can be found that compared with not considering the magnet gravity when the magnet gravity is considered, the acceleration threshold value of the system showing a large response is significantly reduced. The larger the end magnet mass M_e, the smaller the acceleration threshold value of the system. In addition, it can be found that with the increase of M_e, the large RMS voltage of the system also increases gradually.

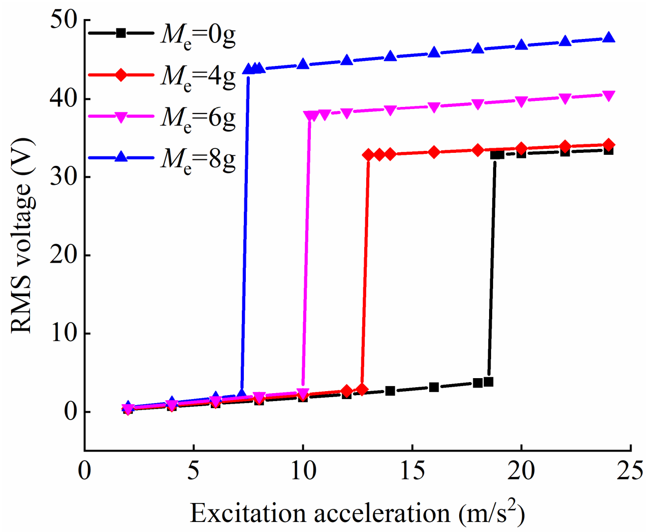

Figure 8. Excitation acceleration threshold of the system under different M_e.

To further analyze the effect of M_e on the system's dynamic characteristics, take A = 10 m/s^2, f = 10 Hz, and M_e take 4 g and 8 g, respectively. The 3D time domain simulation results of the system are shown in Figure 9a,b, where the bottom projection shows the time–displacement diagram of the system, the left projection shows the time–velocity diagram of the system, and the right projection shows the phase diagram of the system. When M_e = 4 g, as shown in Figure 9a, the kinetic energy derived by the system is not enough to pass the potential barrier, the system can only oscillate slightly in the well, and the system's vibration velocity and displacement are small at this time. When M_e = 8 g, as shown in Figure 9b, the increase in the magnet's mass makes the system sufficient kinetic energy, and the system can readily pass the potential barrier to realize an inter-well oscillation. At the moment, the system's vibration velocity and displacement are large. In addition, it can be found that the phase diagram of the system shows a significant asymmetric feature after considering the gravitational effect of the end magnet; the vibration displacement of the system is also asymmetric about the origin. The displacement amplitude in the negative orientation of the system is bigger than that in the positive orientation. This is consistent with the results of the potential energy analysis above.

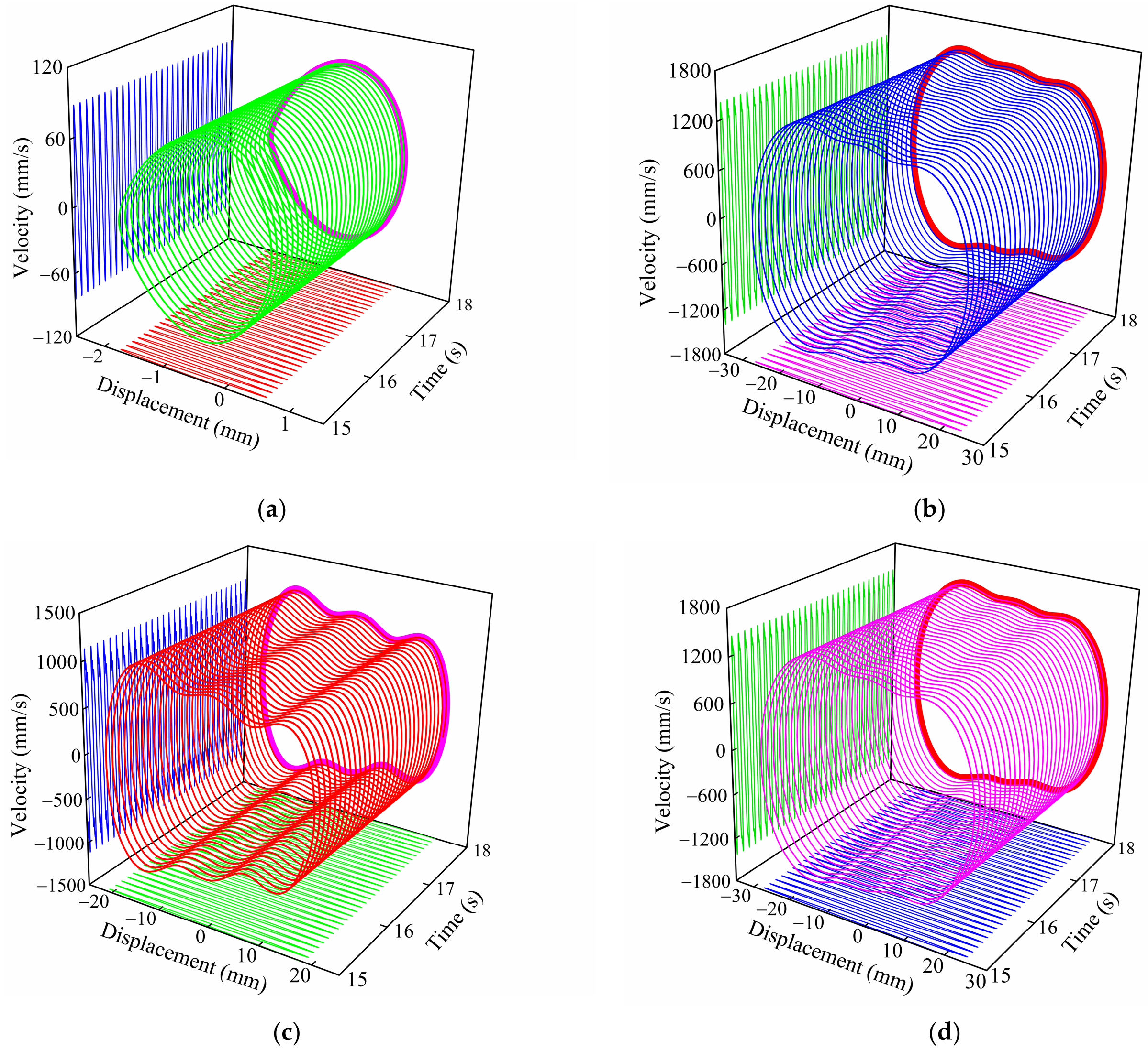

Figure 9. 3D time domain simulation diagram of the system under different M_e, and A: (**a**) M_e = 4 g A = 10 m/s^2; (**b**) M_e = 8 g A = 10 m/s^2; (**c**) M_e = 4 g A = 14 m/s^2; (**d**) M_e = 8 g A = 14 m/s^2.

Keeping other parameters constant, change the excitation acceleration A to 14 m/s^2. As shown in Figure 9c, when M_e = 4 g, the system derives sufficient kinetic energy to pass the potential barrier and achieve a large oscillation of the tri-stable state due to the increase of the vibration acceleration. Compared with Figure 9a, the vibration velocity and displacement are greatly improved at this time. As shown in Figure 9d, when M_e = 8 g, the system can more readily traverse the potential barrier to realize large-amplitude oscillations between wells. Comparing Figure 9b,d, it can be found that the system's vibration velocity and displacement increase as the excitation acceleration increases. Figure 9d, compared with 9c, shows that the larger the end magnet mass, the larger the vibration velocity and displacement of the system for the same initial excitation conditions. However, the large magnet mass will make the vibration displacement of the system too large, which may cause the combined beam to be damaged during the movement. Therefore, it is essential to select the appropriate end magnet mass for actual use.

3.3.2. Influence of Initial Vibration Point u_0 on System Response Characteristics

As can be seen from Figure 7, when the gravity of the end magnet is considered, the left potential well of the tri-stable system incrementally falls and the right potential well incrementally rises, and the potential energy curve exhibits asymmetric characteristics.

Next, under the consideration of the gravity of the magnet, the influence of initial vibration points on the system's output characteristics is studied. Take the vibration frequency f = 10 Hz, d_h = 12 mm, d_v = 16 mm, M_e = 10 g, the initial velocity of the system is 0, and the initial vibration point u_0 is −14, −1, and 12 mm, respectively (that is, the lowest point of the three potential wells). Figure 10 shows the change law of the system's RMS voltage with the vibration acceleration A under different u_0. From Figure 10, it can be found that the excitation acceleration threshold for the system to produce high-energy output is different when the initial vibration point u_0 of the system is different. When u_0 is −14 mm, the acceleration threshold for the system to produce high-energy output is 12.8 m/s^2. When u_0 is −1 and 12 mm, the acceleration threshold of the system is reduced to 8.2 m/s^2 and 8 m/s^2, respectively. In addition, it can be found that the output voltage when the system realizes a large response is consistent regardless of the stable balance point from which the oscillation starts.

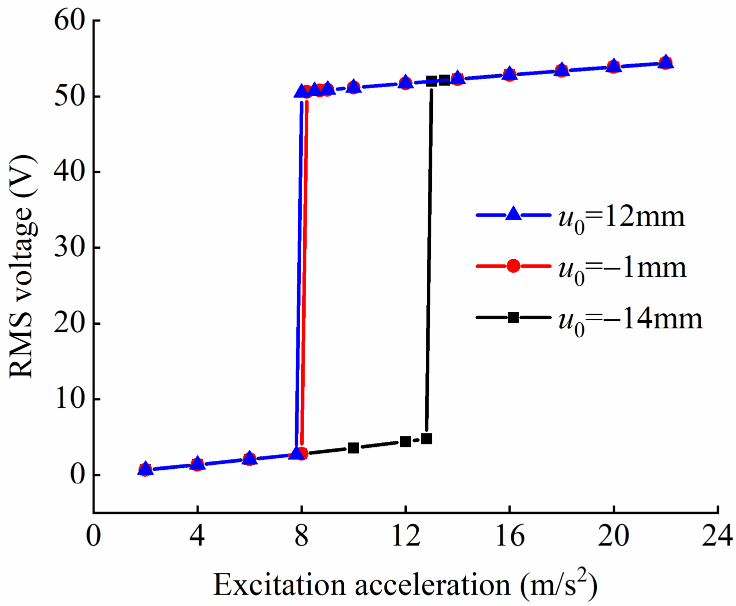

Figure 10. Excitation acceleration threshold of the system under different u_0.

To further study the effect of the initial vibration point u_0 on the response characteristics of the system, take A = 9 m/s^2, f = 10 Hz, M_e = 10 g, and the initial vibration point u_0 is −14 mm and 12 mm, respectively. The 3D time domain simulation results of the system are shown in Figure 11a,b. When u_0 is −14 mm, as shown in Figure 11a, the system is situated in a large potential trough and cannot escape the bondage of the potential trough. Therefore, the system can only perform intra-well oscillation, and the response velocity and displacement at this time are relatively small. When u_0 is 12 mm, as shown in Figure 11b, the system is situated in a small potential trough, which can readily escape the confinement of the potential trough, thereby realizing a large oscillation between the wells. At the moment, the system's vibration velocity and displacement are relatively large.

Keeping other initial parameters unchanged, improve the excitation acceleration A to 13 m/s^2. As shown in Figure 11c, when u_0 is −14 mm, the excitation acceleration at the moment reaches the acceleration threshold of the system's large response. Therefore, the system realizes the large periodic oscillation of the tri-stable state, and the response velocity and displacement both show large amplitude. As shown in Figure 11d, when u_0 is 12 mm, the system also performs periodic oscillation between wells under the excitation acceleration at this time. In addition, the comparison between Figure 11b,d can again show that increasing the initial vibration acceleration can improve the system's vibration velocity and displacement with the same other initial parameters.

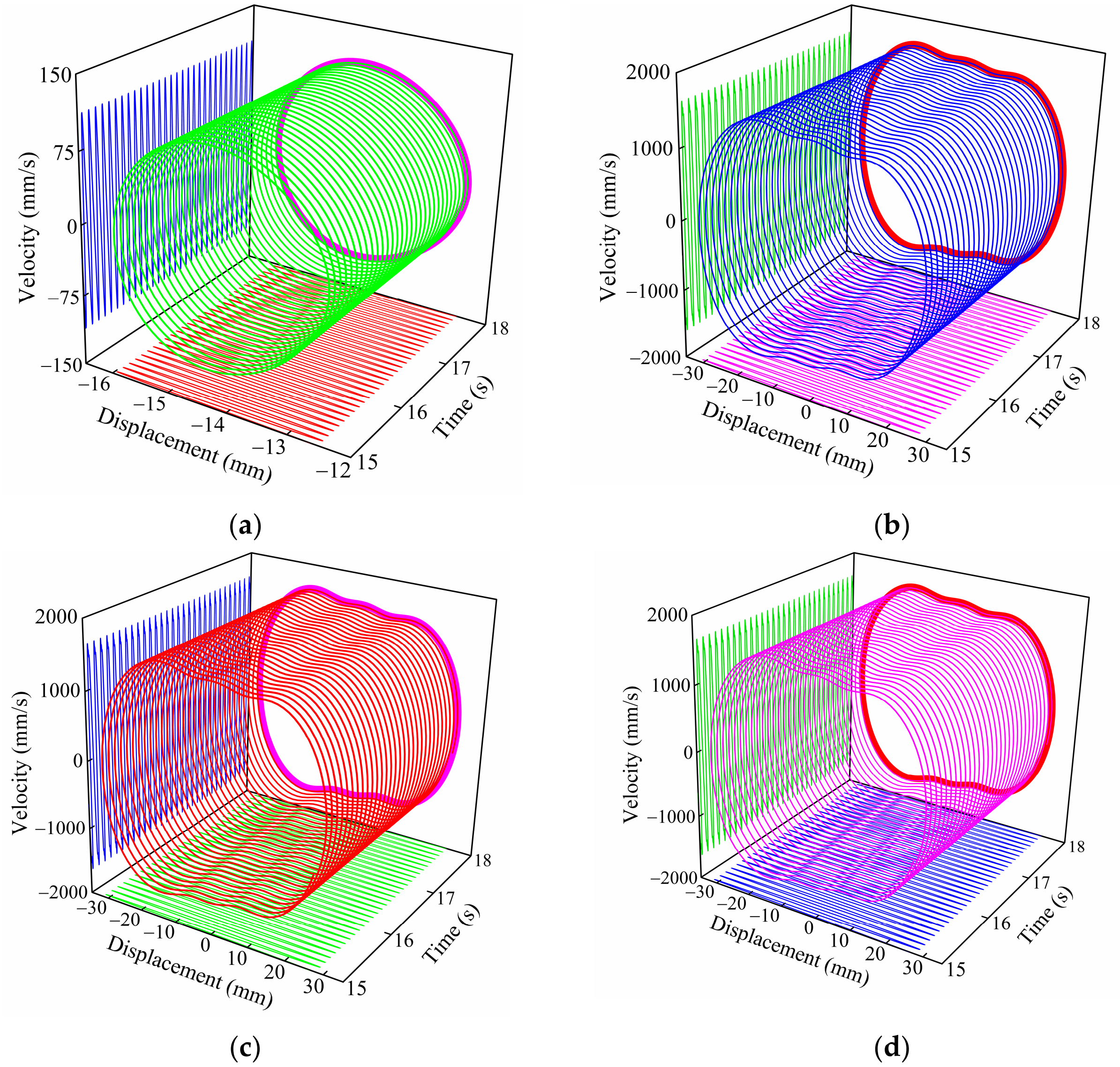

Figure 11. 3D time domain simulation diagram of the system under different u_0 and A: (**a**) $u_0 = -14$ mm $A = 9$ m/s^2; (**b**) $u_0 = 12$ mm $A = 9$ m/s^2; (**c**) $u_0 = -14$ mm $A = 13$ m/s^2; (**d**) $u_0 = 12$ mm $A = 13$ m/s^2.

4. Experimental Validation

In order to validate the rightness of the mathematical model and simulation study, the experiment model machine is fabricated, and the experiment testing platform is built into this research. Figure 12 shows the experimental prototype of CTEHS. The combined beam is made of beryllium bronze material and is machined in one piece. The right end of the beam is clipped and fastened to the pedestal with a fixture, and the left end is glued with a magnet. The top and bottom surfaces of the PVDF piezoelectric film are welded with wires and packaged with insulating tape, and then the treated piezoelectric film is attached to the combined beam with silicone sealant. Two magnets are bonded symmetrically on the left inner wall of the pedestal. The pedestal is provided with several guide rails and chutes, which can be used to regulate the spacing among these magnets.

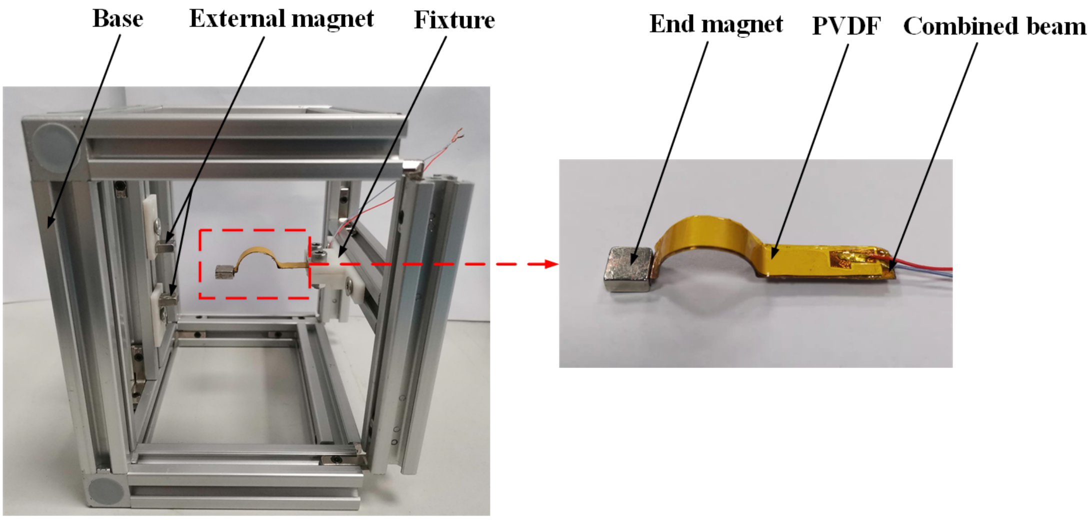

Figure 12. Experiment model machine of CTEHS.

Figure 13 shows the experiment testing platform of the system. When the experiment is conducted, the experiment model machine is first fixed to the shaker (LT-50ST) by screws, then the vibration parameters are configured by the control software, and the vibration signals are transmitted to the shaker controller (VT-9008), then the vibration signals are magnified by the power amplifier (VSA-L1000A) and passed to the shaker to make the experiment model machine on the shaker vibrate. The end velocity and displacement of the combined beam are gauged by a laser vibrometer (LV-S01) and recorded using a vibration analyzer (CoCo-80X). The response voltage of the system is displayed and collected by a digital oscilloscope (DSOX3024T).

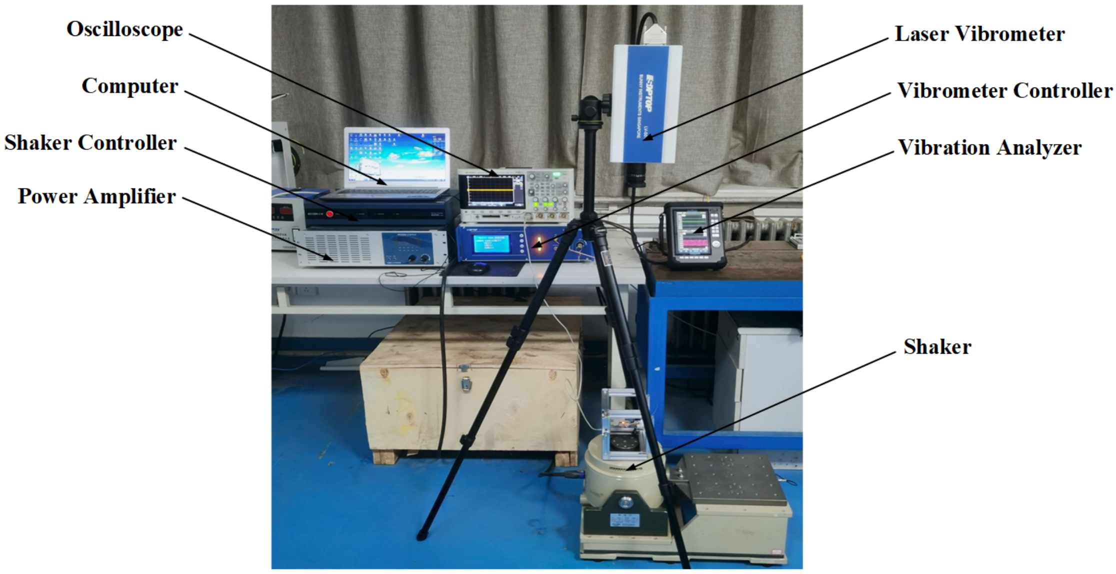

Figure 13. Experiment testing system.

To verify the effect of different end magnet masses M_e on the system's response characteristics, set the vibration frequency $f = 10$ Hz, the vibration acceleration $A = 10$ m/s^2, and take the magnet distances $d_h = 12$ mm and $d_v = 15$ mm. Figure 14 shows the phase graph, time course graph of the experiment when M_e is 4 g and 8 g, respectively. As shown in Figure 14a, when $M_e = 4$ g, the system cannot pass the potential barrier and can only make small oscillations in the well. At this time, the system's vibration displacement amplitude is just 1.8 mm, and the RMS voltage is just 2.48 V. When $M_e = 8$ g, as shown in Figure 14b, the system can surmount the obstacle of the potential barrier and realize a large-amplitude oscillation between wells. The system's vibration displacement amplitude achieves 28 mm, and the RMS voltage reaches 46.38 V. In addition, it can be seen from Figure 14 that the system's vibration displacement and voltage are asymmetric about the origin, which indicates that the motion of the system under the gravity of the magnet is asymmetric. This is consistent with the results of the simulation analysis.

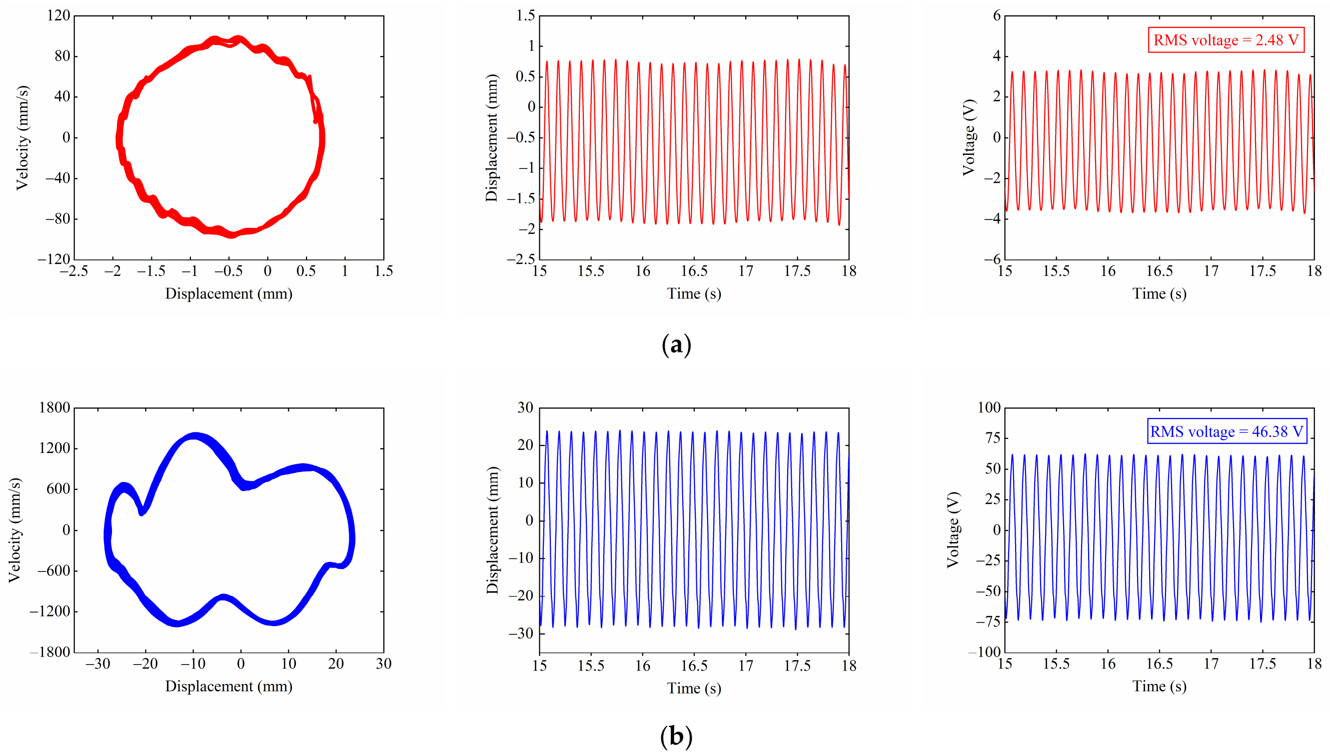

Figure 14. Phase graph, time course graph of the experiment under different M_e: (**a**) M_e = 4 g; (**b**) M_e = 8 g.

To verify the effect of different initial vibration points u_0 on the system's response characteristics, take the magnet distances d_h = 12 mm and d_v = 16 mm, the end magnet mass M_e = 10 g, set the vibration frequency f = 10 Hz and the vibration acceleration $A = 9$ m/s^2. Figure 15 shows the phase graph, time course graph of the experiment when u_0 is −14 mm and 12 mm, respectively. When u_0 =−14 mm, as shown in Figure 15a, the system is unable to get rid of the constraints of the deeper potential well and can only do intra-well periodic oscillations. At this time, the system's vibration displacement amplitude is just 2.1 mm and the RMS voltage is just 3.41 V. As shown in Figure 15b, when u_0 = 12 mm, the system is able to readily pass the lower potential barrier and perform inter-well periodic oscillation. The system's vibration displacement amplitude is increased to 32 mm, and the RMS voltage achieves 49.66 V.

The above experiment results have a fine consistency with the theoretical calculations qualitatively, but there are some deviations in quantitative terms. The main sources of these deviations are: (1) In the experimental prototype, there is a slight error in the size of the fabricated magnet and the combined beam with the simulation. (2) The tension and compression deformation of the arched part of the combined beam is neglected in the theoretical modeling, while the deformation of the arched part also generates some displacement during the actual oscillation, which results in some errors between the actual displacement and the theoretically calculated displacement.

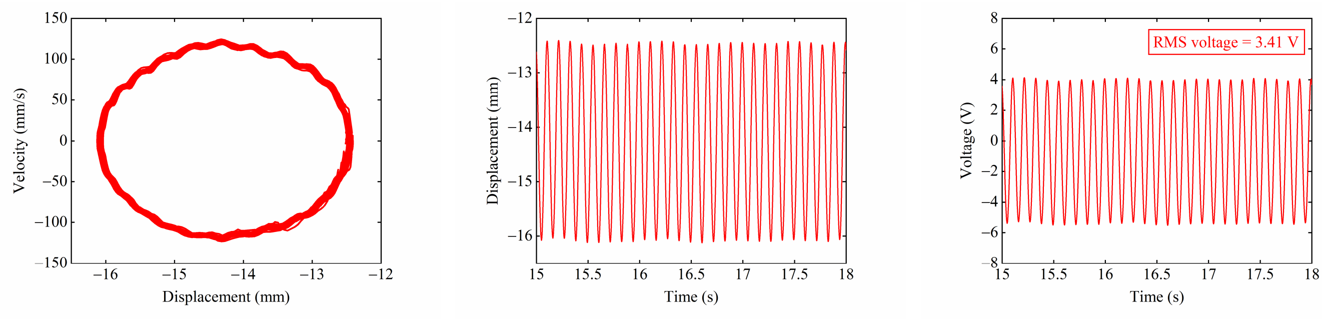

(**a**)

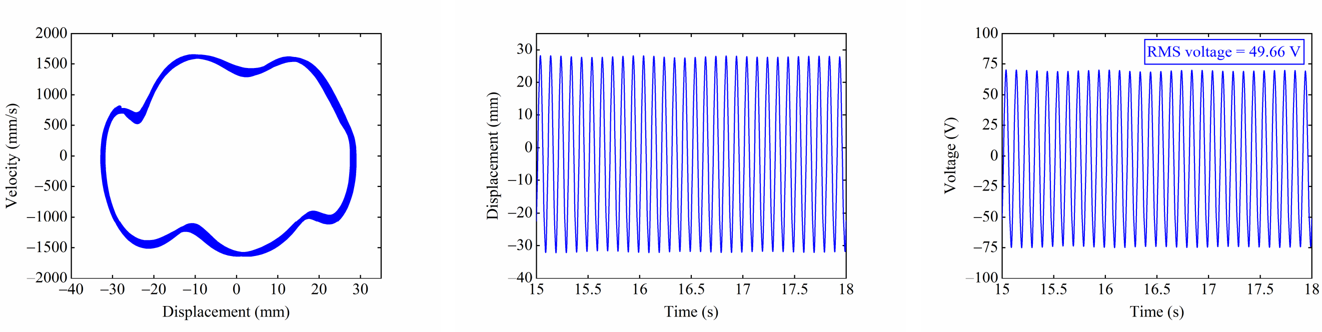

(**b**)

Figure 15. Phase graph, time course graph of the experiment under different u_0: (**a**) u_0 =−14 mm; (**b**) u_0 = 12 mm.

5. Conclusions

In this paper, the mathematical model of CTEHS is established considering the gravity effect of the magnet, and the influences of the end magnet mass and the initial vibration point on the system's static bifurcation and output characteristics are investigated by the method of numeric calculation, and experiments are carried out to validate the theoretical analysis. The major findings of the research are described below:

(1) The gravity of the end magnet has a considerable influence on the system's static bifurcation behavior. With the increase of the end magnet mass M_e, the downward shift of the stable middle position of the system becomes more and more obvious, and the upper and lower stable positions also show significant asymmetry. In addition, the saddle and bifurcation points in the bifurcation diagram move under the gravity of the end magnets, which makes the range of different systems' stable states change, and the system's response characteristics change accordingly.

(2) When the gravity of the end magnet is considered, the system generates additional gravitational potential energy, which causes the system's potential energy graph to show asymmetry. When the mass M_e of the end magnet is increased, the potential well on one side of the system gradually moves down and the depth increases, and the potential well on the other side gradually moves up and decreases in depth, and the asymmetric characteristics of the potential energy curve are more obvious.

(3) The end magnet mass M_e has a remarkable impact on the system's response characteristics. Considering the gravity effect of the magnets can significantly reduce the excitation acceleration required for the system to realize higher output capability. As the end magnet mass M_e increases, the acceleration threshold of the system gradually decreases, and the response displacement and output voltage gradually increase. The gravity effect of the magnet can make it easier for the system to perform large inter-well oscillations at low excitation intensities, thereby increasing the system's energy capture efficiency.

(4) When the initial vibration point u_0 of the system is different, the system's output characteristics are also different. When the system starts to vibrate from a stable equilibrium

point with a deeper potential well, the acceleration threshold for the system to achieve a large response is high. When the system starts from a stable equilibrium point with a shallower potential well, the acceleration threshold for a large response is relatively low. The suitable initial vibration point is beneficial to reduce the system's requirement for external excitation intensity, thus greatly enhancing the system's performance in harvesting energy.

Author Contributions: Conceptualization, X.Z. and H.X.; methodology, H.X.; software, J.P. and X.C.; validation, F.Z. and Y.G.; writing—original draft preparation, H.X.; writing—review and editing, H.T.; visualization, Y.C.; supervision, H.X.; project administration, X.Z.; funding acquisition, X.Z. All authors have read and agreed to the published version of the manuscript.

Funding: This research was funded by the National Natural Science Foundation of China (Grant No.51974228), Shaanxi Coal Joint Fund Project (Grant No.2021JLM-03), Shaanxi Innovative Talent Plan Project (Grant No.2018TD-032), and Key R&D project in Shaanxi (Grant No.2018ZDCXL-GY-06-04).

Institutional Review Board Statement: Not applicable.

Informed Consent Statement: Not applicable.

Data Availability Statement: Not applicable.

Acknowledgments: Authors acknowledge the support from the students Luyang Chen, Yan Guo, and Yujun Cheng for their assistance in the modeling and experiments.

Conflicts of Interest: The authors declare no conflict of interest.

References

1. Muduli, L.; Mishra, D.P.; Jana, P.K. Application of wireless sensor network for environmental monitoring in underground coal mines: A systematic review. *J. Netw. Comput. Appl.* **2018**, *106*, 48–67. [CrossRef]
2. Lei, X.; Wu, Y. Research on mechanical vibration monitoring based on wireless sensor network and sparse Bayes. *EURASIP J. Wirel. Commun.* **2020**, *2020*, 225. [CrossRef]
3. Kafi, M.A.; Challal, Y.; Djenouri, D.; Doudou, M.; Bouabdallah, A.; Badache, N. A Study of Wireless Sensor Networks for Urban Traffic Monitoring: Applications and Architectures. *Procedia Comput. Sci.* **2013**, *19*, 617–626. [CrossRef]
4. Tang, X.; Wang, X.; Cattley, R.; Gu, F.; Ball, A.D. Energy Harvesting Technologies for Achieving Self-Powered Wireless Sensor Networks in Machine Condition Monitoring: A Review. *Sensors* **2018**, *18*, 4113. [CrossRef]
5. Wei, C.; Jing, X. A comprehensive review on vibration energy harvesting: Modelling and realization. *Renew. Sustain. Energy Rev.* **2017**, *74*, 1–18. [CrossRef]
6. Saadon, S.; Sidek, O. A review of vibration-based MEMS piezoelectric energy harvesters. *Energy Convers. Manag.* **2011**, *52*, 500–504. [CrossRef]
7. Safaei, M.; Sodano, H.A.; Anton, S.R. A review of energy harvesting using piezoelectric materials: State-of-the-art a decade later (2008–2018). *Smart Mater. Struct.* **2019**, *28*, 113001. [CrossRef]
8. Yang, Z.; Zhou, S.; Zu, J.; Inman, D. High-Performance Piezoelectric Energy Harvesters and Their Applications. *Joule* **2018**, *2*, 642–697. [CrossRef]
9. Lumentut, M.F.; Howard, I.M. Analytical and experimental comparisons of electromechanical vibration response of a piezoelectric bimorph beam for power harvesting. *Mech. Syst. Signal Process.* **2013**, *36*, 66–86. [CrossRef]
10. Upadrashta, D.; Yang, Y. Finite element modeling of nonlinear piezoelectric energy harvesters with magnetic interaction. *Smart Mater. Struct.* **2015**, *24*, 45013–45042. [CrossRef]
11. Zhang, Y.; Tang, L.; Liu, K. Piezoelectric energy harvesting with a nonlinear energy sink. *J. Intell. Mater. Syst. Struct.* **2017**, *28*, 307–322. [CrossRef]
12. Zhang, H.; Sui, W.; Yang, C.; Zhang, L.; Song, R.; Wang, J. An asymmetric magnetic-coupled bending-torsion piezoelectric energy harvester: Modeling and experimental investigation. *Smart Mater. Struct.* **2021**, *31*, 15037. [CrossRef]
13. Wang, S.; Chen, Z.; Wang, Z.; Xie, Z.; Gong, Y.; Gao, Y.; Huang, W. A magnetically coupled two-degrees-of-freedom piezoelectric energy harvester using torsional spring. *J. Intell. Mater. Syst. Struct.* **2022**, *33*, 2346–2356. [CrossRef]
14. Hu, G.; Tang, L.; Das, R.; Marzocca, P. A two-degree-of-freedom piezoelectric energy harvester with stoppers for achieving enhanced performance. *Int. J. Mech. Sci.* **2018**, *149*, 500–507. [CrossRef]
15. Liu, S.; Cheng, Q.; Zhao, D.; Feng, L. Theoretical modeling and analysis of two-degree-of-freedom piezoelectric energy harvester with stopper. *Sens. Actuators A Phys.* **2016**, *245*, 97–105. [CrossRef]
16. Chen, Y.; Yan, Z. Nonlinear analysis of axially loaded piezoelectric energy harvesters with flexoelectricity. *Int. J. Mech. Sci.* **2020**, *173*, 105473. [CrossRef]
17. Qian, F.; Zhou, S.; Zuo, L. Approximate solutions and their stability of a broadband piezoelectric energy harvester with a tunable potential function. *Commun. Nonlinear Sci.* **2020**, *80*, 104984. [CrossRef]

18. Jiang, J.; Liu, S.; Feng, L.; Zhao, D. A Review of Piezoelectric Vibration Energy Harvesting with Magnetic Coupling Based on Different Structural Characteristics. *Micromachines* **2021**, *12*, 436. [CrossRef]
19. Hou, C.; Shan, X.; Zhang, L.; Song, R.; Yang, Z. Design and Modeling of a Magnetic-Coupling Monostable Piezoelectric Energy Harvester Under Vortex-Induced Vibration. *IEEE Access* **2020**, *8*, 108913–108927. [CrossRef]
20. Fan, K.; Tan, Q.; Liu, H.; Zhang, Y.; Cai, M. Improved energy harvesting from low-frequency small vibrations through a monostable piezoelectric energy harvester. *Mech. Syst. Signal Process.* **2019**, *117*, 594–608. [CrossRef]
21. Harne, R.L.; Wang, K.W. A review of the recent research on vibration energy harvesting via bistable systems. *Smart Mater. Struct.* **2013**, *22*, 23001. [CrossRef]
22. Wang, H.; Tang, L. Modeling and experiment of bistable two-degree-of-freedom energy harvester with magnetic coupling. *Mech. Syst. Signal Process.* **2017**, *86*, 29–39. [CrossRef]
23. Zhou, S.; Lallart, M.; Erturk, A. Multistable vibration energy harvesters: Principle, progress, and perspectives. *J. Sound Vib.* **2022**, *528*, 116886. [CrossRef]
24. Yang, T.; Cao, Q. Dynamics and high-efficiency of a novel multi-stable energy harvesting system. *Chaos Soliton. Fract.* **2020**, *131*, 109516. [CrossRef]
25. Xie, Z.; Huang, B.; Fan, K.; Zhou, S.; Huang, W. A magnetically coupled nonlinear T-shaped piezoelectric energy harvester with internal resonance. *Smart Mater. Struct.* **2019**, *28*, 11LT01. [CrossRef]
26. Wang, C.; Zhang, Q.; Wang, W. Low-frequency wideband vibration energy harvesting by using frequency up-conversion and quin-stable nonlinearity. *J. Sound Vib.* **2017**, *399*, 169–181. [CrossRef]
27. Jiang, J.; Liu, S.; Zhao, D.; Feng, L. Broadband power generation of piezoelectric vibration energy harvester with magnetic coupling. *J. Intell. Mater. Syst. Struct.* **2019**, *30*, 2272–2282. [CrossRef]
28. Fan, K.; Tan, Q.; Zhang, Y.; Liu, S.; Cai, M.; Zhu, Y. A monostable piezoelectric energy harvester for broadband low-level excitations. *Appl. Phys. Lett.* **2018**, *112*, 123901. [CrossRef]
29. Xie, Z.; Zhou, S.; Xiong, J.; Huang, W. The benefits of a magnetically coupled asymmetric monostable dual-cantilever energy harvester under random excitation. *J. Intell. Mater. Syst. Struct.* **2019**, *30*, 3136–3145. [CrossRef]
30. Ferrari, M.; Ferrari, V.; Guizzetti, M.; Andò, B.; Baglio, S.; Trigona, C. Improved energy harvesting from wideband vibrations by nonlinear piezoelectric converters. *Sens. Actuators A Phys.* **2010**, *162*, 425–431. [CrossRef]
31. Erturk, A.; Inman, D.J. Broadband piezoelectric power generation on high-energy orbits of the bistable Duffing oscillator with electromechanical coupling. *J. Sound Vib.* **2011**, *330*, 2339–2353. [CrossRef]
32. Lan, C.; Qin, W. Enhancing ability of harvesting energy from random vibration by decreasing the potential barrier of bistable harvester. *Mech. Syst. Signal Process.* **2017**, *85*, 71–81. [CrossRef]
33. Zhou, S.; Cao, J.; Inman, D.J.; Lin, J.; Liu, S.; Wang, Z. Broadband tristable energy harvester: Modeling and experiment verification. *Appl. Energy* **2014**, *133*, 33–39. [CrossRef]
34. Jung, J.; Kim, P.; Lee, J.; Seok, J. Nonlinear dynamic and energetic characteristics of piezoelectric energy harvester with two rotatable external magnets. *Int. J. Mech. Sci.* **2015**, *92*, 206–222. [CrossRef]
35. Sun, S.; Leng, Y.; Su, X.; Zhang, Y.; Chen, X.; Xu, J. Performance of a novel dual-magnet tri-stable piezoelectric energy harvester subjected to random excitation. *Energy Convers. Manag.* **2021**, *239*, 114246. [CrossRef]
36. Zhou, Z.; Qin, W.; Zhu, P. Harvesting performance of quad-stable piezoelectric energy harvester: Modeling and experiment. *Mech. Syst. Signal Process.* **2018**, *110*, 260–272. [CrossRef]